PHOTONICS Research

Local boundary modulation of photonic antichiral edge states

SHIYU LIU,[1,†] YUTING YANG,[1,5,†] WEIPENG LI,[1] LIWEI SHI,[1] ENYUAN WANG,[2] GUIGENG LIU,[3,6] AND ZHIHONG HANG[4,7]

[1]School of Materials and Physics, China University of Mining and Technology, Xuzhou 221116, China
[2]School of Safety Engineering, China University of Mining and Technology, Xuzhou 221116, China
[3]Department of Electronic and Information Engineering, School of Engineering, Westlake University, Hangzhou 310030, China
[4]School of Physical Science and Technology & Collaborative Innovation Center of Suzhou Nano Science and Technology, Soochow University, Suzhou 215006, China
[5]e-mail: yangyt@cumt.edu.cn
[6]e-mail: liuguigeng@westlake.edu.cn
[7]e-mail: zhhang@suda.edu.cn
[†]These authors contributed equally to this work.

Received 10 March 2026; revised 19 May 2026; accepted 20 May 2026; posted 21 May 2026 (Doc. ID 597176); published 16 July 2026

The antichiral edge states in the modified Haldane model have been extensively studied, revealing intriguing pairs of co-propagating edge states alongside complementary bulk states. In this work, we investigate how local modulations lift the degeneracy of the original antichiral edge states and give rise to pronounced transport phenomena. Amplitude modulation of the hopping terms on the zigzag edges leads to the deformed dispersions of the antichiral edge states, creating an energy imbalance between the two edges. Directional modulation of the hopping terms on the zigzag edges induces twisted dispersions that support the bidirectional edge state propagation. Modulation of the on-site potential energy on one edge leads to the half-antichiral edge states, where propagation occurs exclusively along a single edge. These phenomena are realized using gyromagnetic photonic crystals and confirmed through experimental measurements. By locally controlling magnetization and geometric structure, the antichiral edge state transport provides a practical platform for tunable multichannel waveguides, opening new avenues for the implementation of topological photonic devices.

https://doi.org/10.1364/PRJ.597176

1. INTRODUCTION

In recent years, topological insulators have enabled robust backscattering-immune edge state transport by leveraging nontrivial topological properties [1–4]. Inspired by the quantum Hall effect, the classical Haldane model (HM) breaks time-reversal symmetry, constructing chiral edge states protected by a non-zero Chern number [5–9]. Subsequently, the modified Haldane model (mHM) has been proposed in which the two Dirac points shift to distinct frequencies—one upward and the other downward—giving rise to antichiral edge states that co-propagate along opposite system boundaries, while reverse transport compensation emerges in the bulk states propagating in the opposite direction [10–20]. Even when the frequencies of the edge state dispersions overlap with those of the bulk bands, these edge states maintain robustness against local defects and sharp bends.

Recent studies have focused on enhancing the controllability of topological edge states. Strain engineering applied to the HM and mHM [21] can induce the structural deformation together with the shift of Dirac points, equivalent to modulating the hopping between neighboring lattice sites, thereby generating a synthetic gauge field [22,23]. Interlayer coupling in the bilayer HM or mHM with A-A or A-B stacking cases gives rise to distinct topological phase transitions [24–28]. In addition to global regulation of the system, the chiral edge states in the HM can be manipulated through the on-site potential on the zigzag edges that relies on local configuration of edge geometry within the photonic crystals [29]. The modulation of the antichiral edge states under the side potential has been studied in electronic systems [30–32]; however, it is unexplored in the classical wave system. Our work further extends to modulate the side-hopping terms and realize them in the photonic crystal. Moreover, in contrast to the local modulation in the HM [29], our proposed local modulation including both on-site potential and hopping terms in the mHM, brings out abundant physical phenomena and transport properties of antichiral edge states.

This work proposes and experimentally demonstrates a strategy of local boundary modulation (Fig. 1) that changes the hopping term and the on-site potential energy in the

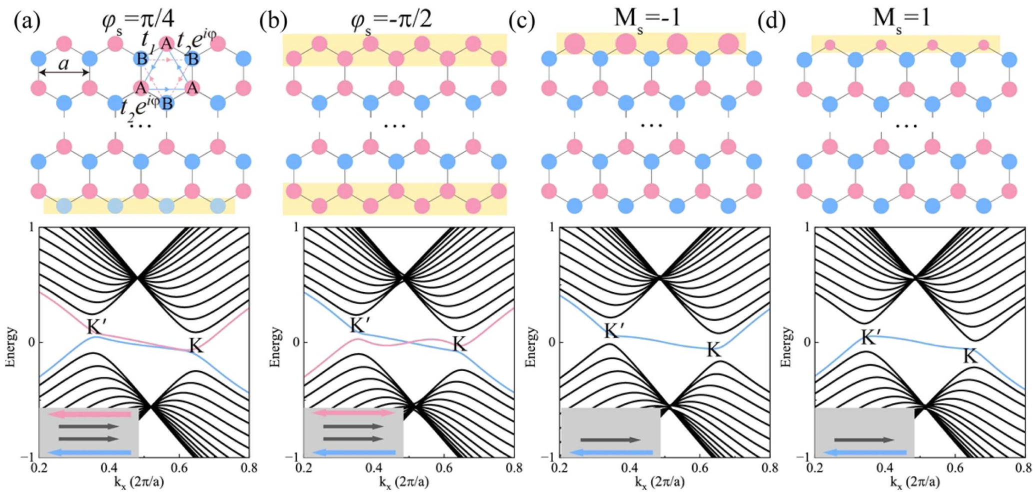

Fig. 1. Schematic of the tight-binding model and band structures. Sublattices A and B are represented by the red and blue circles in the schematic diagrams. The local modulation regions are marked by the yellow shading. Antichiral edge states on the upper and lower boundaries are represented by the red and blue curves. Insets illustrate the corresponding transport of the edge states. t_1 and t_2 are the NN and NNN hopping amplitudes, respectively. φ and φ_s are NNN hopping phases on the global and local structures, respectively. M and M_s denote the global and the on-site potential energies on the top edge, respectively. $t_1 = 1$ and $t_2 = 0.03$. (a) $M = 0$, $\varphi = \pi/2, \varphi_s = \pi/4$; (b) $M = 0$, $\varphi = \pi/2, \varphi_s = -\pi/2$; (c) $M = 0$, $\varphi = \pi/2$, $M_s = -1$; (d) $M = 0$, $\varphi = \pi/2$, $M_s = 1$.

mHM, enabling independent control of two antichiral edge states on upper and lower zigzag boundaries. Through modulation of the local magnetization intensity and direction, as well as the geometric structure of the gyromagnetic photonic crystals (GPCs), we lift the degeneracy of the antichiral edge states to induce controllable band structures. Distinct from conventional global modulation, this approach enables directional tunability of the propagation direction and energy intensity of the upper and lower antichiral edge states. We further propose a design of a multichannel waveguide, offering a feasible pathway for realizing highly flexible photonic devices.

2. RESULTS

A. Tight-Binding Model

In the modified Haldane model, the antichiral edge states are achieved. The Hamiltonian of its tight-binding model is

$$H = t_1 \sum_{<i,j>} c_i^\dagger c_j + t_2 \sum_{\ll i,j \gg} e^{-iv_{ij}\varphi} c_i^\dagger c_j + M \sum_i c_i^\dagger c_i,$$

where $c_i^\dagger$ (c_i) is the creation (annihilation) operators at site i; $<i,j>$ and $\ll i,j \gg$ run over all the nearest-neighbor (NN) and next-nearest-neighbor (NNN) hopping sites. t_1 and t_2 are NN and NNN hoppings, respectively, and φ represents the global hopping phase. $v_{ij} = 1$ (−1) indicates the counterclockwise (clockwise) hopping direction between sublattices A, while $v_{ij} = -1$ (1) represents that between sublattices B. M represents the on-site potential energy. The Bloch Hamiltonian after the Fourier transform is

$$H = \begin{pmatrix} M + H_{11} & H_0 \\ H_0^* & -M + H_{22} \end{pmatrix},$$

where $H_0 = t_1 \sum_{i=1,2,3} e^{i\vec{k}\cdot\vec{\alpha}_i}$ and $H_{11} = H_{22} = 2t_2 \sum_{i=1,2,3} \cos(\varphi - \vec{k}\cdot\vec{v}_i)$. $\vec{\alpha}_i$ represents the displacements from a B site to its three adjacent A sites, and $\vec{v}_1 = \vec{\alpha}_2 - \vec{\alpha}_3$, $\vec{v}_2 = \vec{\alpha}_3 - \vec{\alpha}_1$, $\vec{v}_3 = \vec{\alpha}_1 - \vec{\alpha}_2$. Two degenerate antichiral edge states with identical group velocities and the associated bulk bands are displayed in Appendix A.

Building on the modified Haldane model, we tune the NNN hopping terms on the zigzag boundaries. The Hamiltonian is

$$H = t_1 \sum_{<i,j>} c_i^\dagger c_j + t_2 \sum_{\ll i,j \gg}^{w-s} e^{-iv_{ij}\varphi} c_i^\dagger c_j + t_2 \sum_{\ll i,j \gg}^{s} e^{-iv_{ij}\varphi_s} c_i^\dagger c_j,$$

where φ_s denotes the modulated NNN hopping phase at the zigzag boundaries and the global on-site potential M is set to zero. The parameter w denotes the width of the whole structure, and the s indicates the width of the modified hopping phase on the upper or lower boundaries. As shown in Fig. 1(a), when the NNN hopping phases are $\varphi = \pi/2$ on the global structure and $\varphi_s = \pi/4$ on the bottom boundary, the degeneracy of the original edge state dispersions is lifted. The dispersion of the upper edge retains its original slope, while the dispersion of the lower edge is deformed and shifts overall toward lower energies (detailed band evolution in Fig. 7 in Appendix B). As $\varphi_s = -\pi/2$ on the top and bottom boundaries, the lower edge dispersion undergoes significant distortion, exhibiting coexisting positive and negative slopes, as shown in Fig. 1(b). The bulk bands remain unchanged throughout the modulation of the NNN hopping.

Next, we investigate the modulation of the local on-site potential energy on the zigzag edges as illustrated in Figs. 1(c) and 1(d). The Hamiltonian is

$$H = t_1 \sum_{<i,j>} c_i^\dagger c_j + t_2 \sum_{\ll i,j \gg} e^{-iv_{ij}\varphi} c_i^\dagger c_j + \sum_i^{w-s} M c_i^\dagger c_i + \sum_i^{s} M_s c_i^\dagger c_i.$$

The site potential energy M_s can be modulated on the upper or lower boundaries. In Figs. 1(c) and 1(d), as M_s gradually increases (decreases) from 0 to 1 (−1), the degenerate energy bands of the upper and lower edge states gradually lift: the dispersion curve of the upper edge state shifts upward (downward), eventually merging into the bulk bands and vanishing (see Appendix B, Fig. 8 for details). Adjusting the local on-site potential energy selectively shifts an edge-state frequency at a chosen boundary into (or out of) the bulk band, thereby enabling independent control of the transport channel on that boundary.

B. Modulation of the Hopping Term in the Photonic System

The photonic implementation of the modified Haldane model is realized using GPCs, enabling the antichiral transport along the zigzag boundaries. The three-dimensional schematic of the experimental setup is illustrated in Fig. 2(a). The lattice constant of the honeycomb GPC is $a = 10$ mm. The yttrium iron garnet (YIG) cylinders at sublattices A and B have a radius of $r = 0.15a$ and a height of $d = 5$ mm. Sublattices A and B are subjected to magnetization intensities of $H = 0.13$ T in opposite directions, as indicated by the white arrows. This structural configuration induces strong anisotropy in the YIG cylinders, leading to the permeability tensor (see Appendix A for details). The detailed experimental method is explained in Appendix C. While GPCs enable robust antichiral edge state transport, their intrinsic properties result in the two edge states being degenerate due to reliance on the global magnetization of the A and B sublattices. This global dependence impedes independent regulation of individual edge states. The modulation of the NNN hopping on the zigzag boundaries is achieved by tuning the magnetization intensity of the GPC cylinders at specific sublattices. As illustrated in Fig. 2(b), the degeneracy of the edge state dispersions is lifted in numerical calculations under a specific magnetic field strength of $H_s = -0.08$ T. This localized magnetization modulation exerts a pronounced effect exclusively on targeted edges, such as the lower edge, without altering the dispersion characteristics of the opposing edge state or the bulk band structure, thereby fully demonstrating the independent control capability inherent to our design. Further, as shown in Fig. 2(c), tuning the external magnetic field intensity on the site allows us to precisely manipulate the dispersion curves of the lower edge states. As the magnetic field increases, the group velocity of the lower edge states decreases gradually. Meanwhile, we find that the frequency of the dispersion curve shifts toward the lower frequency regime. The detailed band evolution is shown in Fig. 9 in Appendix D.

We perform the experiments to validate the aforementioned theory and demonstrate the practical transport characteristics of the deformed edge states. The excited antichiral edge states propagate leftward along the waveguide. The excited sources are dipole antennas, placed on the right side of the upper and lower boundaries of the GPC sample, indicated by the yellow stars in Figs. 2(d) and 2(e). Experimental results exhibit a frequency shift of approximately 0.1 GHz toward higher frequencies relative to numerical simulations, owing to the influence of material fabrication errors and losses. Near 9.4 GHz, we observe that the electric field intensity at the upper edge is significantly stronger than that at the lower edge. This finding is further confirmed by the transmission coefficients measured at the output ports P_1 and P_2 within the yellow regions:

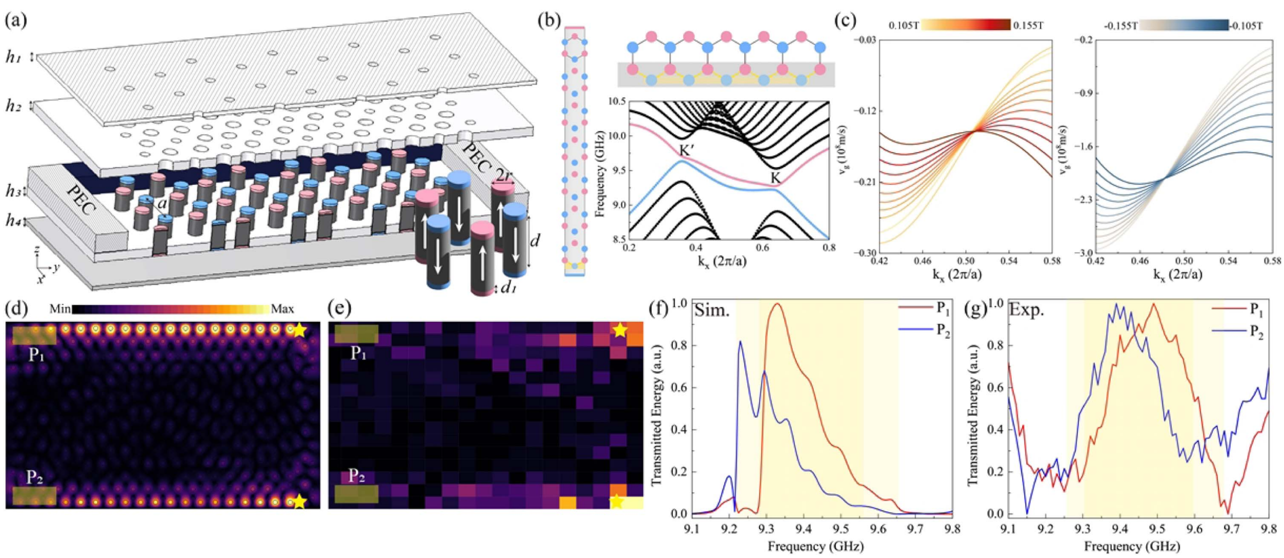

Fig. 2. (a) Schematic of the experimental setup for observing antichiral edge states transport in the GPCs. The YIG cylinders with radius $r = 0.15a$ and height $d = 5$ mm are embedded in a waveguide consisting of two parallel metallic plates. The permanent magnets of the same radius r and height $d_1 = 0.5$ mm are tightly attached above and below each YIG cylinder. The external magnetic field is $H_A = -H_B = 0.13$ T. The thicknesses of the four metallic plates are $h_1 = h_4 = 1$ mm and $h_2 = h_3 = 2$ mm, respectively. The inset shows the GPC cylinders, with white arrows indicating magnetization directions. (b) Left panel: schematic of the supercell and modulation of the magnetization intensities with $H_s = -0.08$ T on the bottom boundary. Right panel: numerically simulated antichiral edge states with the deformed band dispersions, where the upper and lower edge state dispersions are denoted by red and blue lines, respectively. (c) Group velocity of the lower edge dispersion curves under different magnetization intensities H_s. (d) and (e) Simulated and experimentally measured electric field distributions of the unbalanced edge states at 9.45 and 9.375 GHz, respectively. (f) and (g) Simulated and measured transmission spectra of output ports P_1 and P_2, respectively.

modulated by the local magnetic biasing, the dispersion curves of the antichiral edge states undergo distortion. This distortion induces asymmetric energy distribution between the upper and lower boundaries while altering the frequency range of the electromagnetic wave propagation compared to the upper edge.

After investigating the band deformation through introducing NNN hopping modulation via one side of the GPCs, we further explore the impact of modulation on both sides, leading to the twisted edge state dispersions. As illustrated in Fig. 3(a), the external magnetic fields applied to the top and bottom boundaries are opposite relative to their original orientations. The projected bands reveal that, compared to the original modified Haldane model, the degeneracy of the antichiral edge states is lifted: the upper edge dispersion exhibits coexisting positive and negative group velocities, while the lower edge remains less affected and retains its original leftward propagation. Eigenfield distributions show that, at the same frequency, the upper edge hosts two bulk states (states 1 and 5) and three distinct edge states (states 2–4) simultaneously. Figure 3(b) compares the edge state transport characteristics under two-sided modulation, obtained from numerical simulations and experimental measurements. Placing the excitation source at the center of the upper edge enables simultaneous excitation of the leftward and rightward propagating electromagnetic waves. For the bulk modes, only rightward propagation is excited, as shown in Figs. 3(c) and 3(d). The pronounced unidirectional propagation of the system is directly verified by comparing the transmission spectra S_1 (rightward propagation) with S_2 (leftward propagation) in Fig. 3(e).

C. Modulation of the On-Site Potential in the Photonic System

This section explores how modulating the on-site potential energy on the zigzag edges, corresponding to tuning the geometric size of the GPC system, affects the antichiral edge state transport. The top views of the experimental samples are shown in Figs. 4(a_1) and 4(a_2). Changing the radius r_s of the GPC cylinders at the top boundary lifts the original degeneracy in the band dispersion and simultaneously shifts the frequency of the respective edge states upward or downward, eventually leading to the half-antichiral edge state, which propagates only along one edge. The band dispersions of the half-antichiral edge states are displayed in Figs. 4(b_1) and 4(b_2), in which the radii of cylinders at the top edge are $r_s = 0.1a$ and $0.2a$, respectively. Figure 10 in Appendix D displays the detailed band evolution during the changing of the radius r_s. When the radii r_s decrease (increase), the upper edge dispersion shifts toward the high (low) frequency and eventually merges into the bulk bands and vanishes, while the lower edge retains edge state transport. To verify the above conclusions, we conduct microwave experiments, as shown in Figs. 4(c_1) and 4(c_2). When the excitation sources are placed at the upper and lower edges, the measured

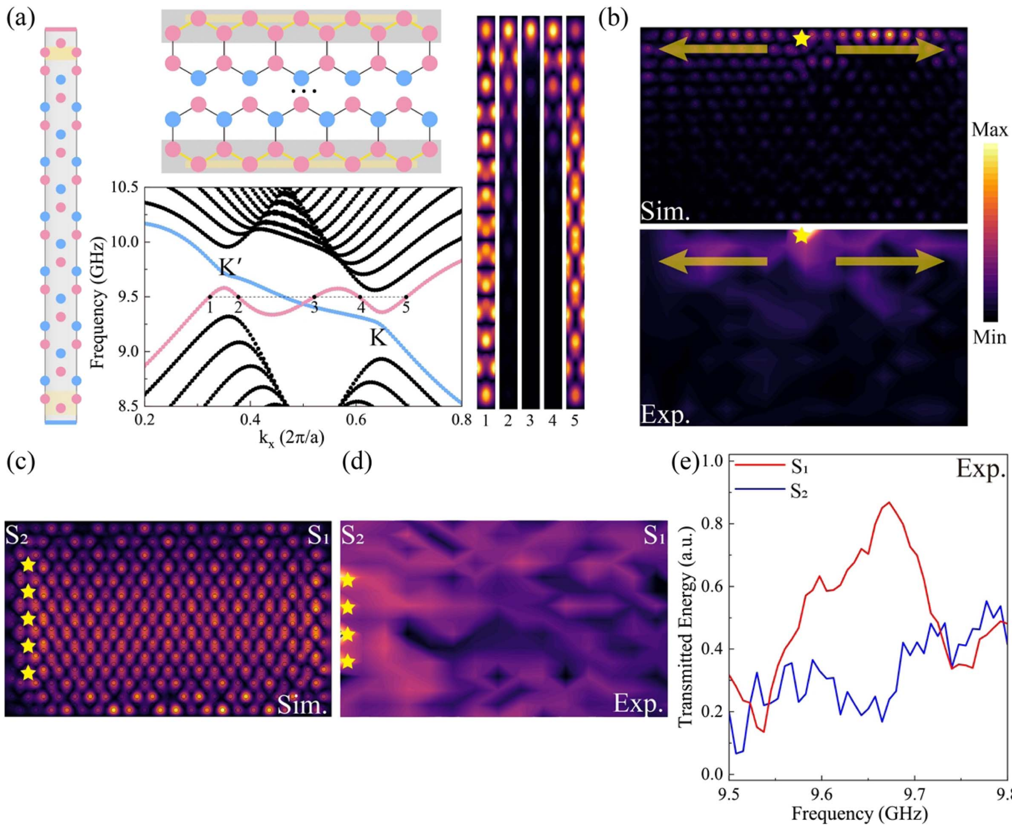

Fig. 3. (a) Band structure of numerically simulated antichiral edge states with twisted band dispersions under the two-sided modulation of the magnetization direction. Right panel: electric field distributions of five eigenstates. (b) Simulated and experimentally measured electric field distributions at 9.49 and 9.63 GHz, respectively. Yellow stars denote the positions of excitation sources. (c) and (d) Simulated and experimentally measured electric fields of the bulk modes at 9.61 and 9.65 GHz. (e) Experimentally measured transmission spectra of ports S_1 and S_2, respectively.

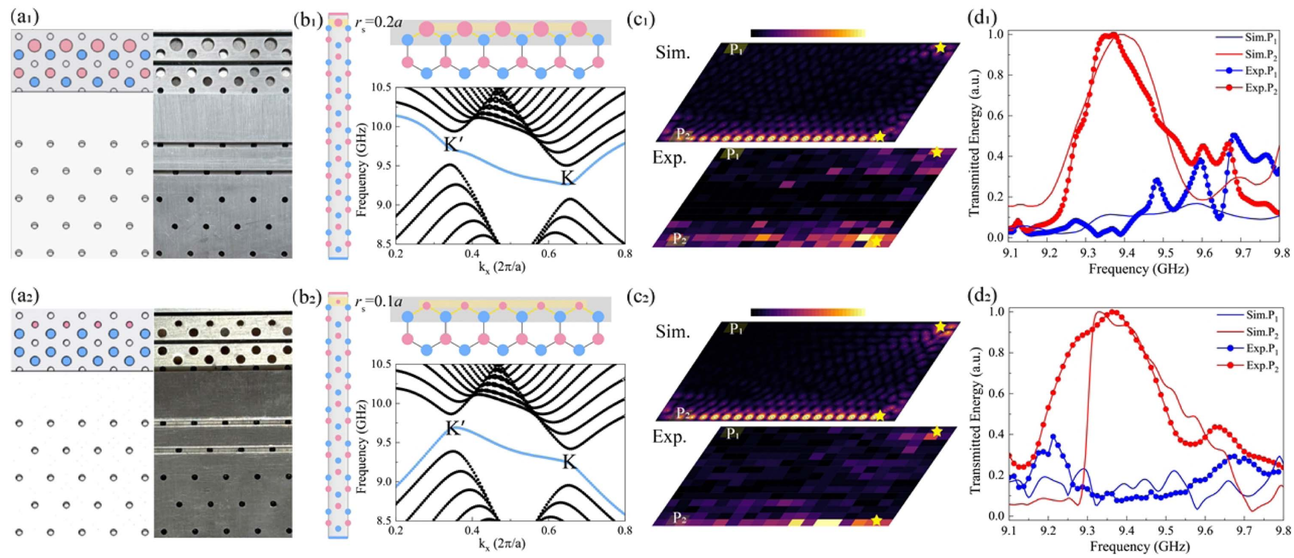

Fig. 4. Regulation characteristics and experimental verification of the half-antichiral edge states under the radius variation of the YIG cylinders at the top boundary: (a_1)–(d_1) $r_s = 0.2a$; (a_2)–(d_2) $r_s = 0.1a$. The other GPC parameters are consistent with those in Fig. 2. (a_1) and (a_2) Top view of the simulated and experimental setups. (b_1) and (b_2) Numerically calculated band structure of the half-antichiral edge states. (c_1) and (c_2) Simulated and experimentally measured electric field distributions of the half-antichiral edge states at 9.38 and 9.4 GHz, respectively for $r_s = 0.2a$ and $0.1a$. (d_1) and (d_2) Simulated and experimentally measured transmission spectra at the detection points P_1 and P_2 for $r_s = 0.2a$ and $0.1a$, respectively.

transmission spectra at the yellow regions (P_1 and P_2) are in good agreement with numerical simulations, as displayed in Figs. 4(d_1) and 4(d_2). The disappearance of the upper edge states, coupled with the nearly unchanged lower edge states, further supports the mechanism through which the modulation of the on-site potential energy controls the edge state transport. The half-antichiral edge states prevent the information crosstalk induced by the unwanted coupling between different states, which pave the way for the designed compact devices.

D. Multichannel Waveguide

We selectively modulate the zigzag boundaries of the GPCs to control the propagation direction and energy distribution of electromagnetic waves, thereby designing a multichannel waveguide. This photonic device is composed of structures I and II, including four output ports P_1–P_4 and one excitation port. As shown in Figs. 5(a_1) and 5(b_1), the top and bottom boundaries of structure II are subjected to the two-sided modulation of the magnetization direction, corresponding to twisted edge state dispersions in Fig. 3. This results in the formation of three-channel waveguides, as shown in Figs. 5(a_2) and 5(b_2). There is no electromagnetic wave emitted from the P_4 port in Fig. 5(a_2) and the P_3 port in Fig. 5(b_2), indicating that the twisted band structure can control the on–off state of the pathways. The geometric size of the bottom (top) boundary of structure I is modulated in Fig. 5(c_1) [Fig. 5(d_1)], while the structure II undergoes two-sided modulation of the magnetization direction, enabling designing two-channel bidirectional waveguides, as displayed in Figs. 5(c_2) and 5(d_2). The band dispersions of the structure I correspond to the half-antichiral edge states in Fig. 4. By adjusting the local parameters within structures I and II, it is possible to accurately customize the on–off state of electromagnetic wave transmission at particular output ports, selectively manage power, and block unnecessary pathways to achieve flexible signal routing and power distribution. This provides a flexible and controllable scheme for the design of photonic devices.

3. CONCLUSION

Based on the modified Haldane model, we modulate the NNN hopping amplitude, hopping direction, and on-site potential energy at the top and bottom zigzag boundaries, thereby lifting the originally degenerate antichiral edge states. The resulting effects include: (i) deformed antichiral edge state dispersions with tunable differences in the group velocity between two band branches; (ii) twisted band dispersions that support bidirectional edge propagation; and (iii) a half-antichiral edge state enabling unidirectional edge transport. These theoretical frameworks are implemented in a photonic system based on GPCs. By tuning the magnetization intensity, magnetization direction, and geometric parameters of the GPC structures, we experimentally demonstrate flexible control over the propagation direction and intensity of the electromagnetic wave. Furthermore, we propose a multichannel waveguide device: by locally adjusting structural parameters, the electromagnetic energy transmission at specific output ports can be accurately tailored, enabling flexible channel routing and power allocation. This design exploits the independent tunability of hopping terms and on-site potential modulation, offering a versatile platform for highly integrated photonic circuits with functional reconfiguration.

APPENDIX A: MODIFIED HALDANE MODEL AND PHOTONIC IMPLEMENTATION

The tight-binding model of the mHM and its antichiral edge state dispersions are illustrated in Fig. 6(a). The photonic implementation of the mHM is realized in the GPCs. The gyromagnetic material of the GPCs is commercially available

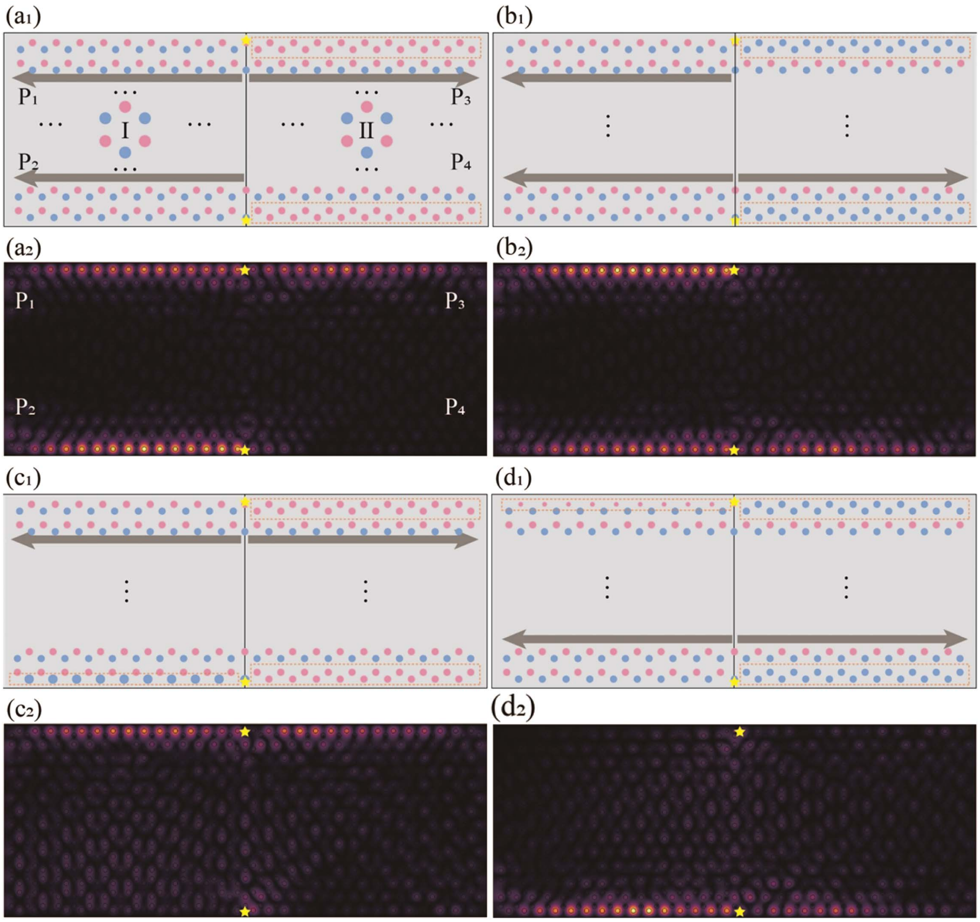

Fig. 5. (a_1)–(d_1) Schematics of the multichannel waveguide. Each multichannel waveguide comprises structures II and I under modulation of the magnetization direction and geometric size of the GPCs, corresponding to the twisted edge states and half-antichiral edge states in Figs. 3 and 4, respectively. The orange dashed box indicates the locally modulated area. (a_2)–(d_2) Simulated electric field distribution at 9.4 GHz for the corresponding structures. The yellow stars mark the excitation location. The output ports are denoted by P_1–P_4.

YIG with the measured relative permittivity 14.5 and the dielectric loss tangent 0.0002. Its measured saturation magnetization is $M_t = 1800$ Gauss, with a ferromagnetic resonance line width of 20 Oe. The magnetization decreases to a negligible value in the absence of the external magnetic field. The relative magnetic permeability of the YIG has the following form:

$$\hat{\mu}_A = \begin{pmatrix} \mu_r & -\mu_k & 0 \\ i\mu_k & \mu_r & 0 \\ 0 & 0 & 1 \end{pmatrix}, \quad \hat{\mu}_B = \begin{pmatrix} \mu_r & i\mu_k & 0 \\ -i\mu_k & \mu_r & 0 \\ 0 & 0 & 1 \end{pmatrix},$$

where $\hat{\mu}_A$ and $\hat{\mu}_B$ correspond to the magnetic permeability tensors of the A and B sublattices, and $\mu_r = 1 + \frac{(\omega_0+i\alpha\omega)\omega_m}{(\omega_0+i\alpha\omega)^2-\omega^2}$, $\mu_k = \frac{\omega\omega_m}{(\omega_0+i\alpha\omega)^2-\omega^2}$, $\omega_m = \gamma M_t$, $\omega_0 = \gamma H_A$. When the external magnetic field applied to the sublattices A and B is $H_A = -H_B = 0.13$ T, $\mu_r = 0.762$ and $\mu_k = -0.622$ are achieved. $\gamma = 1.76 \times 10^{11}\ \mathrm{s^{-1}\,T^{-1}}$ is the gyromagnetic ratio. ω is the operating frequency. The photonic antichiral edge states are shown in Fig. 6(b). Figures 6(c) and 6(d) depict the electric field distribution of the antichiral edge states at the frequency of 9.55 GHz and the bulk state at the frequency of 9.57 GHz, respectively. The excitation sources are placed at the position marked by the yellow stars. Figure 6(e) presents the transmission spectra at the output ports P_1 and P_2 in the simulations. Figure 6(f) shows the transmission curves of the bulk modes. The rightward-propagating bulk modes exceed those of the leftward-propagating modes.

APPENDIX B: ANTICHIRAL EDGE STATES UNDER MODULATION OF THE HOPPING TERM AND ON-SITE POTENTIAL

The band dispersions of the antichiral edge states, deformed by the NNN hopping term at the bottom zigzag boundary, are shown in Fig. 7.

The band evolution of the antichiral edge states under modulation of the on-site potential energy M_s on the top and bottom edges is shown in Fig. 8. For Figs. 8(a)–8(e), the on-site potential of the top boundary is modulated. When M_s decreases from 1 to 0, the upper edge state dispersion detaches from the bulk bands, and the overall frequency decreases until $M_s = 0$, at which point it has the same group velocity as the lower edge dispersion. As M_s decreases from 0 to −1, the frequency of the upper edge dispersion continues

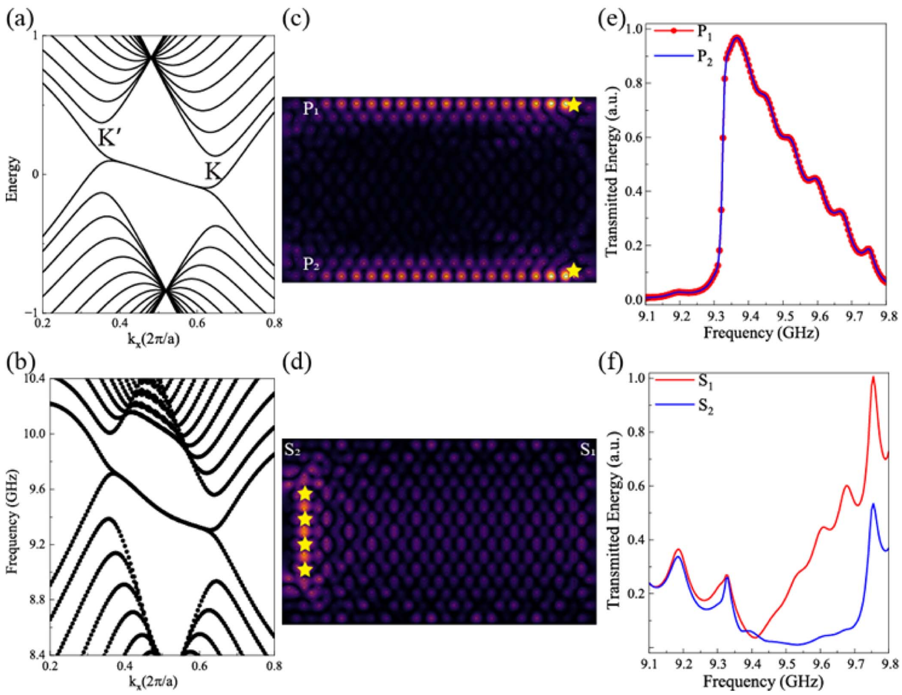

Fig. 6. (a) Antichiral edge state dispersion in the mHM. Parameters: $M = 0$, $t_1 = 1$, $t_2 = 0.03$, and $\varphi = \pi/2$. (b) Photonic antichiral edge state in the GPCs. (c) Electric field distribution of the antichiral edge states at 9.55 GHz. Yellow stars denote the positions of the excitation sources. (d) Electric field distribution of the bulk state at 9.57 GHz. (e) Numerical simulation transmission spectra at the output ports P_1 and P_2. (f) Transmission spectra of the bulk modes at the ports S_1 and S_2.

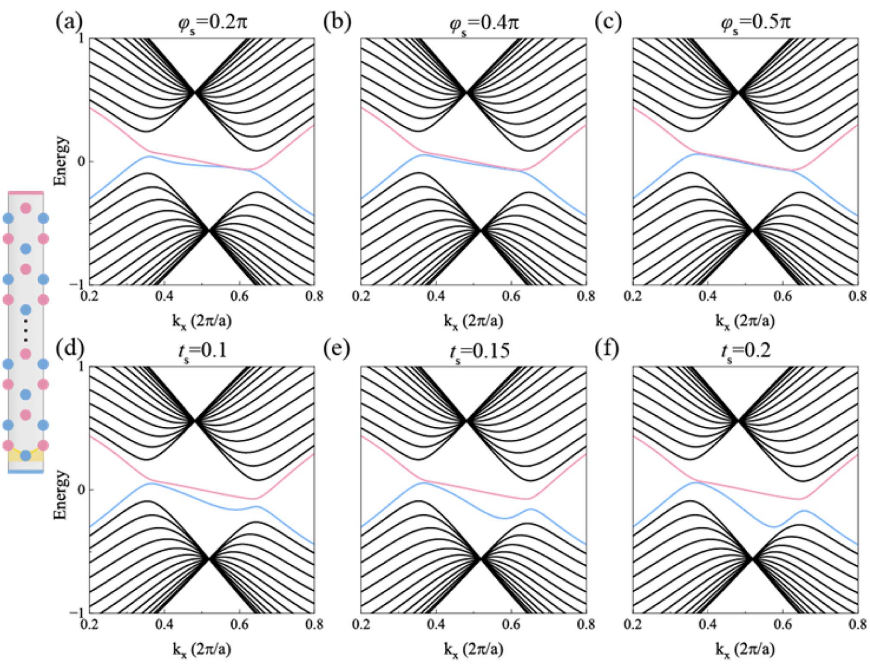

Fig. 7. (a)–(c) Deformed antichiral edge state dispersion associated with modulation of the NNN hopping phase φ_s at the bottom boundary. φ_s varies from 0.2π to 0.5π. (d)–(f) Deformed dispersion curve of the antichiral edge states under modulation of the NNN hopping amplitude t_s at the bottom boundary. The other parameters are same with those in Fig. 1.

to decrease until it sinks into the bulk bands. During this process, the upper edge dispersion remains present with no significant changes. For Figs. 8(f)–8(j), the on-site potential of the bottom boundary is modulated. When M_s decreases from 1 to 0, the lower edge dispersion is raised from the bulk bands until it coincides with the upper edge dispersion curve at $M_s = 0$. As M_s continues to decrease to −1, the lower edge dispersion ultimately completely disappears in the band gap

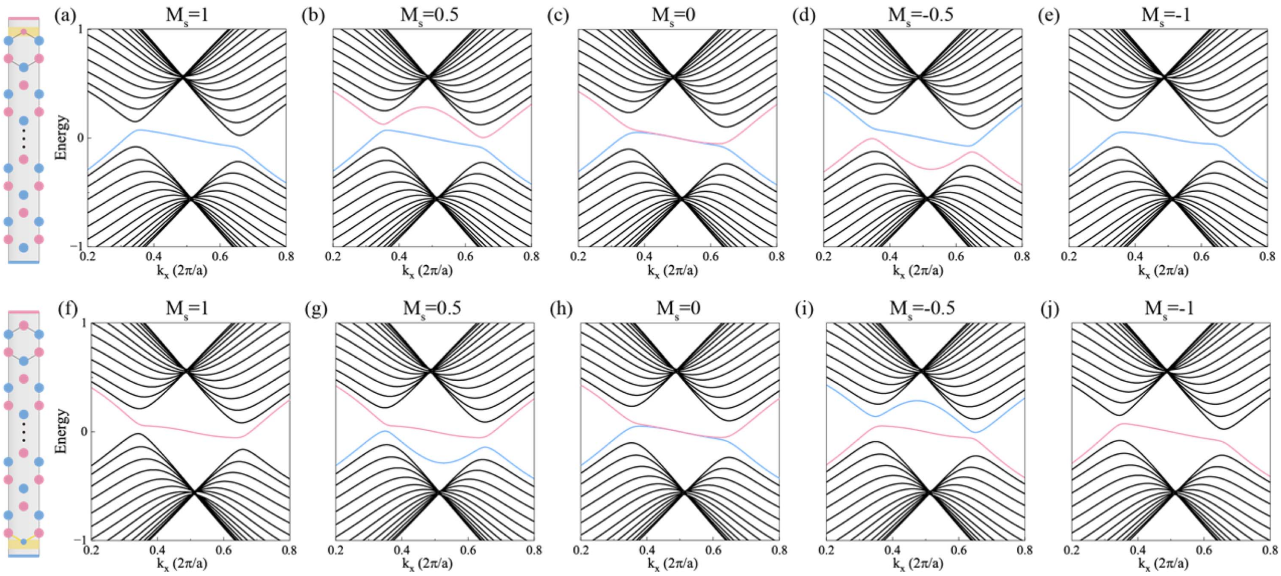

Fig. 8. (a)–(j) Band evolution of the antichiral edge states corresponding to modulation of the on-site potential M_s at the top and bottom boundaries. Inset: the structural schematic.

and merges into the bulk bands. Only the upper edge dispersion exists, and during this process, there are no significant changes in the upper edge dispersion.

APPENDIX C: EXPERIMENTAL METHOD

In the experimental setup, the entire photonic crystal is enclosed within a waveguide composed of two parallel metallic plates. To further prevent electromagnetic wave leakage into the air, the upper and lower surfaces of the structure are additionally covered with metallic plates. For convenient excitation of electromagnetic waves and near-field detection, circular holes are pre-drilled in the top metallic plate. To avoid wave scattering, absorbing materials are employed around the experimental sample. The external magnetic fields applied to the gyromagnetic cylinders are realized by tightly attaching samarium-cobalt

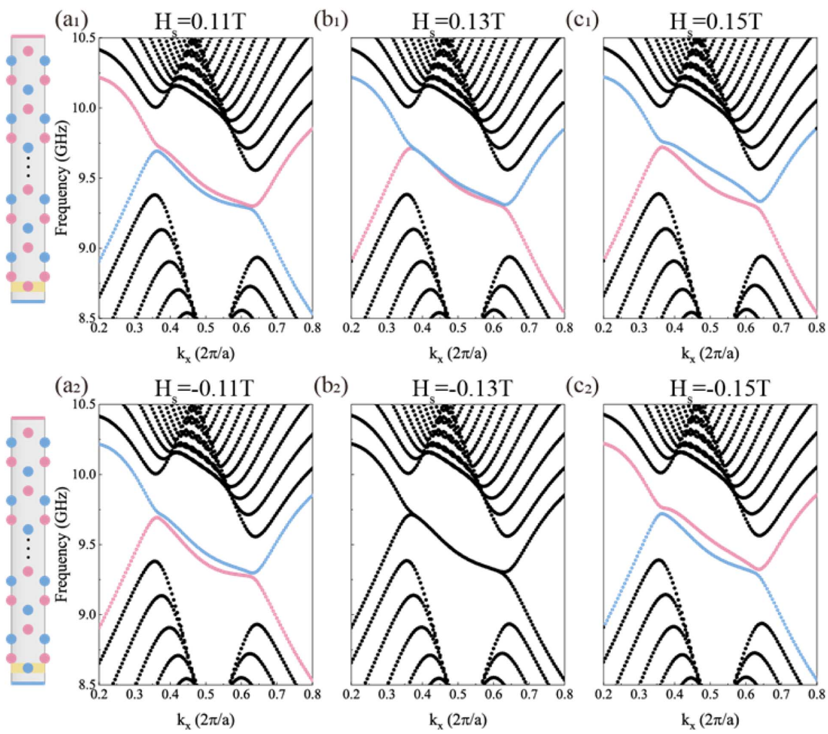

Fig. 9. (a_1)–(c_1) Deformed band structure of the antichiral edge states when the magnetic fields H_s of the bottom boundary are positive, corresponding to z direction. (a_2)–(c_2) Deformed antichiral edge state when the magnetic field H_s of the bottom boundary is negative.

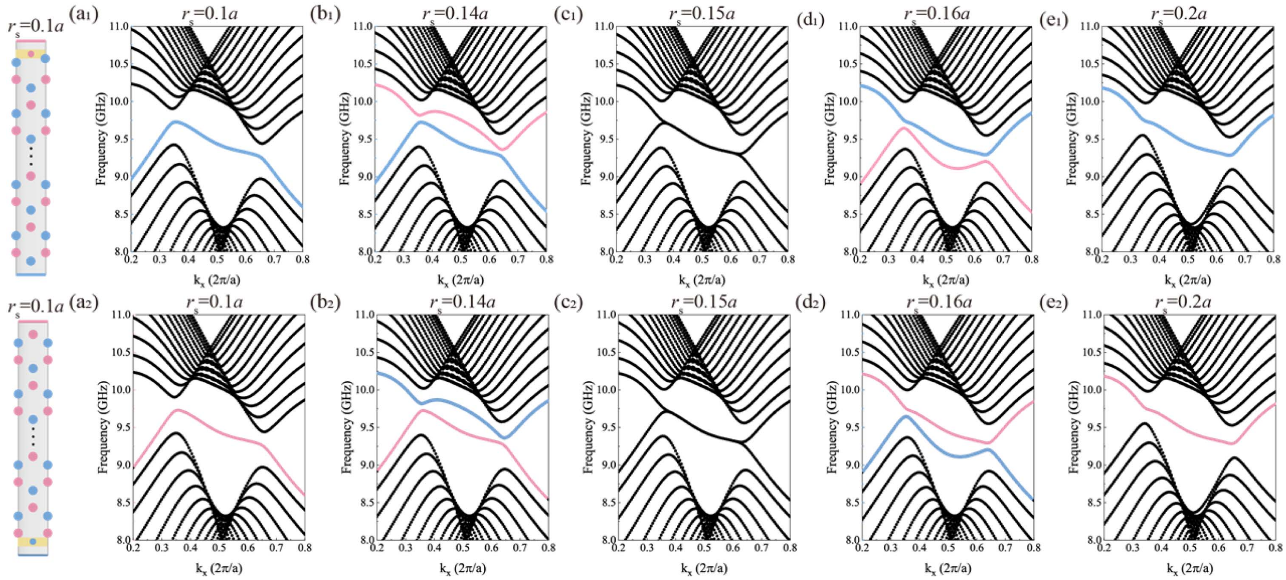

Fig. 10. (a_1)–(e_1) Band evolution of the half-antichiral edge states as r_s changes from $0.1a$ to $0.2a$ at the top boundary. (a_2)–(e_2) Band evolution of the half-antichiral edge states as r_s changes from $0.1a$ to $0.2a$ at the bottom boundary.

(SmCo) permanent magnets to both the top and bottom surfaces of each cylinder. The magnetization intensity of YIG cylinders is controlled by choosing gyromagnetic material and changing the size of permanent magnets.

APPENDIX D: LOCAL BOUNDARY MODULATION IN GYROMAGNETIC PHOTONIC CRYSTALS

The band dispersions of the antichiral edge states are deformed by variation of the magnetization intensity at the bottom boundary, as shown in Fig. 9.

As the values of r_s vary between $0.1a$ and $0.2a$, the edge state dispersions of the top and bottom boundaries gradually transition and eventually merge into the bulk bands, as indicated in Fig. 10.

Funding. National Natural Science Foundation of China (12574477, 52227901, 12274315); Fundamental Research Funds for the Central Universities (2023ZDYQ11003).

Disclosures. The authors declare no conflicts of interest.

Data Availability. Data underlying the results presented in this paper are not publicly available at this time but may be obtained from the authors upon reasonable request.

REFERENCES

1. M. Z. Hasan and C. L. Kane, "Topological insulators," Rev. Mod. Phys. **82**, 3045–3067 (2020).
2. X.-L. Qi and S.-C. Zhang, "Topological insulators and superconductors," Rev. Mod. Phys. **83**, 1057–1110 (2011).
3. T. Ozawa, H. M. Price, A. Amo, *et al.*, "Topological photonics," Rev. Mod. Phys. **91**, 015006 (2019).
4. H. Xue, Y. Yang, and B. Zhang, "Topological acoustics," Nat. Rev. Mater. **7**, 974–990 (2022).
5. F. D. M. Haldane, "Model for a quantum Hall effect without Landau levels: condensed-matter realization of the 'parity anomaly'," Phys. Rev. Lett. **61**, 2015–2018 (1988).
6. N. Jia, C. Owens, A. Sommer, *et al.*, "Time-and site-resolved dynamics in a topological circuit," Phys. Rev. X **5**, 021031 (2015).
7. S. Raghu and F. D. M. Haldane, "Analogs of quantum-Hall-effect edge states in photonic crystals," Phys. Rev. A **78**, 033834 (2008).
8. Z. Wang, Y. Chong, J. D. Joannopoulos, *et al.*, "Observation of unidirectional backscattering-immune topological electromagnetic states," Nature **461**, 772–775 (2009).
9. Y. Poo, R.-X. Wu, Z. Lin, *et al.*, "Experimental realization of self-guiding unidirectional electromagnetic edge states," Phys. Rev. Lett. **106**, 093903 (2011).
10. E. Colomés and M. Franz, "Antichiral edge states in a modified Haldane nanoribbon," Phys. Rev. Lett. **120**, 086603 (2018).
11. Y. Yang, D. Zhu, Z. H. Hang, *et al.*, "Observation of antichiral edge states in a circuit lattice," Sci. China Phys. Mech. Astron. **64**, 257011 (2011).
12. J. Chen, W. Liang, and Z.-Y. Li, "Antichiral one-way edge states in a gyromagnetic photonic crystal," Phys. Rev. B **101**, 214102 (2020).
13. P. Zhou, G.-G. Liu, Y. Yang, *et al.*, "Observation of photonic antichiral edge states," Phys. Rev. Lett. **125**, 263603 (2020).
14. J.-W. Liu, F.-L. Shi, K. Shen, *et al.*, "Antichiral surface states in time-reversal-invariant photonic semimetals," Nat. Commun. **14**, 2027 (2023).
15. J. Chen and Z.-Y. Li, "Prediction and observation of robust one-way bulk states in a gyromagnetic photonic crystal," Phys. Rev. Lett. **128**, 257401 (2022).
16. X. Xi, B. Yan, L. Yang, *et al.*, "Topological antichiral surface states in a magnetic Weyl photonic crystal," Nat. Commun. **14**, 1991 (2023).
17. Y.-C. Zhou, H.-S. Lai, J.-L. Xie, *et al.*, "Magnetic corner states in a two-dimensional gyromagnetic photonic crystal," Phys. Rev. B **107**, 014105 (2023).
18. H. Wang, B. Xie, and W. Ren, "Coexistence of chiral and antichiral edge states in photonic crystals," Laser Photonics Rev. **18**, 2300764 (2024).
19. L. Xie, L. Jin, and Z. Song, "Antihelical edge states in two-dimensional photonic topological metals," Sci. Bull. **68**, 255–258 (2023).
20. Y.-C. Zhou, Z.-Q. Sun, H.-S. Lai, *et al.*, "Observation of photonic Chern metal with bi-chiral edge propagation," Laser Photonics Rev. **18**, 2400826 (2024).

21. M. Mannaï and S. Haddad, "Strain tuned topology in the Haldane and the modified Haldane models," J. Phys. Condens. Matter **32**, 225501 (2020).
22. Y.-H. Ho, E. V. Castro, and M. A. Cazalilla, "Haldane model under nonuniform strain," Phys. Rev. B **96**, 155446 (2017).
23. S. Liu, Y. Yang, L. Shi, *et al.*, "Chiral and antichiral edge states in gyromagnetic photonic crystals under magnetic and pseudomagnetic fields," Photonics Res. **13**, 2688–2696 (2025).
24. M. Mannaï, J.-N. Fuchs, F. Piéchon, *et al.*, "Stacking-induced Chern insulator," Phys. Rev. B **107**, 045117 (2023).
25. J.-H. Guan, W.-K. Lou, and K. Chang, "Topological hidden phase transition in honeycomb bilayers with a high Chern number," Phys. Rev. B **110**, 165303 (2024).
26. K. W. Lee, P.-H. Fu, and Y. S. Ang, "Interplay between Haldane and modified Haldane models in α-T_3 lattice: band structures, phase diagrams and edge states," Phys. Rev. B **109**, 235105 (2024).
27. L. Liu, J. An, Y. Ren, *et al.*, "Engineering corner states by coupling two-dimensional topological insulators," Phys. Rev. B **111**, 045403 (2025).
28. S. Mandal, Z. Wang, R. Banerjee, *et al.*, "Photonic bilayer Chern insulator with corner states," Phys. Rev. Lett. **135**, 016903 (2025).
29. J. Chen, Y. Zheng, S. Yang, *et al.*, "One-way valley-robust transport in edge-tailored photonic crystals," Phys. Rev. Lett. **134**, 203803 (2025).
30. J.-E. Yang, X.-L. Lü, and H. Xie, "Modulation of antichiral edge states in zigzag honeycomb nanoribbons by side potentials," Commun. Phys. **6**, 62 (2023).
31. X.-L. Lü and J.-F. Liu, "Generation and edge-state transitions of pseudohelical edge state based on side potentials in graphene," New J. Phys. **26**, 093023 (2024).
32. J.-E. Yang, J.-X. Long, and X.-L. Lü, "Tuning chiral edge state and spin-filtering in irradiated silicene nanoribbons based on side potentials," J. Appl. Phys. **137**, 054301 (2025).